



Stability and Resistance of Hollow Section Steel Beam-Columns

Marielle Hayeck¹, Elsy Saloumi², Joanna Nseir³, Nicolas Boissonnade⁴

Abstract

The present paper reports on deep research investigations towards the direct design of hollow section shape beam-columns by means of the Overall Interaction Concept (O.I.C.). It details how this approach can simply yet effectively handle the influence of both local and global instabilities on the plastic capacity of the member. The results of 12 beam-column tests on members up to 5.0 m are presented, as well as many other ones collected from the literature. Application of the O.I.C. to characterize these experimental results allows to evidence that the concept is capable of directly accounting for the most relevant parameters, as well as of clearly identifying the remaining ones to be accounted for in the reduction factor-slenderness interaction curves. Besides, validated shell F.E. models have been used extensively to gather a pool of numerical reference results, in the perspective of deriving interaction curves for design practice. Results demonstrate that interaction curves shall be made dependent i) of the bending moment distribution, ii) of the cross-section slenderness, iii) of the relative level of axial compression, and iv) of the tube manufacturing process.

1. Introduction

This paper addresses the behavior, resistance and design of steel hollow section members. The intention is here to propose an original design approach based on the Overall Interaction Concept (O.I.C.) (Boissonnade N. 2013). The Overall Interaction Concept makes use of both ‘Resistance’ and ‘Stability’ aspects and includes the influence of initial imperfections (out-of straightness, residual stresses, non-homogenous material) which makes the member’s real resistance results from an interaction between cross-section resistance and instability, as illustrated in Figure 1.

In the proposed approach, cross-sectional and member resistances are based on extended Ayrton-Perry approaches (Ayrton W.E. and Perry J. 1886), providing reduction χ factors that account for potential local and global (member) instabilities. Since continuous strength functions are proposed in the O.I.C. approach, no cross-section classification steps or section effective properties determination are needed. Also, the method is built such that combined load cases can be as easily treated as simple ones.

¹ PhD, <marielle_hayeck@hotmail.com>

² PhD, <elsysaloumi@gmail.com>

³ Professor, Saint-Joseph University, ESIB, <joanna.nseir@usj.edu.lb>

⁴ Professor, Laval University, <nicolas.boissonnade@gci.ulaval.ca>

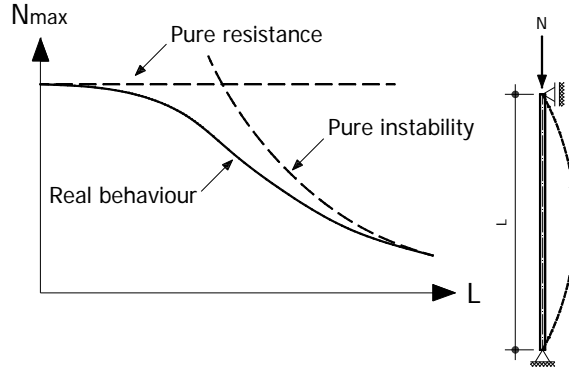


Figure 1: Resistance – stability interaction for flexural buckling

The proposed O.I.C. approach relies on the generalization of the relative slenderness factor defined as $\lambda = \sqrt{R_{RESIST} / R_{STAB}}$, where R_{RESIST} represents the ratio by which the initial loading has to be multiplied to reach the pure resistance limit and R_{STAB} is the equivalent factor used to reach the buckling load (instability) of the ideal member. A relative slenderness value “ λ ” leads to the determination of a “ χ ” value (Figure 2) called “reduction factor” that represents the penalty due to instability effects on the pure resistant behavior.

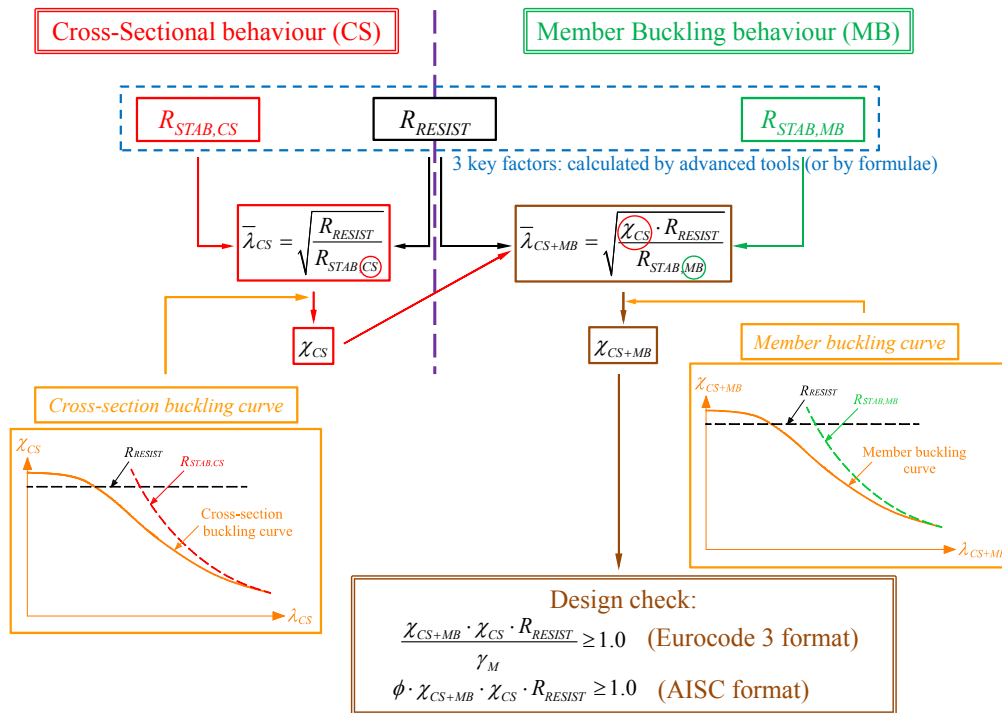


Figure 2: Principles and application steps of proposed “Overall Interaction Concept”

Preliminary research works (Nseir J. 2015) at the cross-sectional level (i) allowed to evidence the suitability and ease of application of the concept, (ii) established a new overall cross-section slenderness λ_{CS} capable of handling plate interactions within the section, (iii) identified the key parameters affecting the resistance in an $\chi_{CS} - \lambda_{CS}$ format at the cross-section level, and (iv) proposed so-called $\chi_{CS} = f(\lambda_{CS})$ resistance functions that were shown to be significantly more accurate and safe than major design codes predictions.

The present paper further extends the application of the O.I.C. to members with hollow section shapes. It addresses their inelastic beam-column response, and include possible local-global interaction under simple and combined loading situations – one of the most complex element's responses.

Many existing such design approaches have been developed in the past decades and have been implemented in design standards (EC3, AISC LRFD, BS 5950, DIN 18 800, AS 4100...). As detailed in (Boissonnade 2006), Eurocode 3 design rules for beam-columns are certainly the most advanced and accurate beam-column formulae; in particular, tubular sections were deeply considered and received specific treatment. Consequently, they have been kept as an analytical reference for the present study.

In the following, the results of experimental, numerical and theoretical investigations are reported. This paper first describes a series of 12 beam-column tests performed on rectangular and circular hollow section shapes. Detailed preliminary measurements are also described in Section 2, such as material and stub column tests, residual stresses and initial geometrical imperfections measurements. Section 3 then reports on the development and validation of purposely-designed shell F.E. models; both the present test series and another series (Semi-Comp 2007) are used as experimental references to assess the F.E. models.

Section 4 further reports on the results of more than 70 000 GMNIA numerical simulations performed on hot-rolled and cold-formed beam-column members, respectively. These results have been further used to characterize the local-global buckling of beam-columns with respect to many parameters, such as cross-section shape (square and rectangular tubes), hot-rolled and cold-formed fabrication processes, different types of loading situations (from simple load cases to combined ones), different element lengths, different steel grades and various cross-section dimensions and thicknesses so as to cover “plastic” to “slender” responses of the sections.

These results are later used to assess the merits of the proposed design approach, and excellent performance is demonstrated, both in terms of accuracy and consistency, which is remarkable given the formal simplicity of the proposed approach.

2. Experimental studies

2.1. Overview of test series

Twelve beams involving 4 different cross-section shapes of nominal steel grade S355 were tested: two hot-rolled **C**ircular **H**ollow **S**ection shapes (CHS 159x5 and CHS 159x6.3) as well as two cold-formed **R**ectangular **H**ollow **S**ection shapes (RHS 200x100x4 and RHS 220x120x6). The columns were loaded under combined compression and bending by varying axial compression load eccentricities e_y and e_z . Two column lengths were chosen so as inelastic buckling to be governing (4000 mm and 4900 mm). Table 1 summarizes the delivered cross-section shapes, their fabrication process and the average values of the measured cross-section dimensions.

Table 1: Measured dimensions of tested specimens

Test #	Cross-section shape	Fabrication process	Measured dimensions			
			H	B	t	D
			(mm)	(mm)	(mm)	(mm)
1	RHS 200x100x4	CF	200.12	100.28	4.00	–
2	RHS 200x100x4	CF	200.42	100.08	4.05	–
3	RHS 200x100x4	CF	198.66	99.93	3.85	–
4	RHS 220x120x6	CF	220.09	119.77	5.90	–
5	RHS 220x120x6	CF	219.91	120.27	5.86	–
6	RHS 220x120x6	CF	219.90	119.78	5.83	–
7	CHS 159x5	HR	–	–	5.42	159.80
8	CHS 159x5	HR	–	–	5.30	159.30
9	CHS 159x5	HR	–	–	5.30	159.40
10	CHS 159x6.3	HR	–	–	6.51	159.20
11	CHS 159x6.3	HR	–	–	6.53	159.40
12	CHS 159x6.3	HR	–	–	6.40	159.20

Preliminary measurements of material properties, geometrical imperfections, residual stresses as well as stub column tests are reported within the present paper. The (imperfect) initial geometry of each specimen was measured along the whole column by means of two different procedures. The first method relied on the use of a set of equally spaced **L**inear **V**ariable **D**isplacement **T**ransducers (**LVDTs**) displaced on each specimen's plates; the second method consisted in scanning the specimen's plates by means of a laser Tracker *AT401*. Residual stresses were also examined experimentally: the sectioning technique was used to get the deformations of the released material; these results have been compared to measurements taken with electrical strain gauges.

Further to the results of the tests themselves, the main goal was here to collect sufficient information for the validation of F.E. numerical tools, in order to launch extensive numerical parametric studies on hot-rolled and cold-formed sections, including a wide scope of parameters (such as cross-section shape, steel grade, load case...). Also, additional test data from European project "Semi-Comp" (Semi-Comp 2007) have been added to the present results, cf. §2.6 – this project aimed at determining the influence of semi-compact class 3 sections on member buckling behavior and included similar beam-column experiments. The experimental results were compared to the results of the F.E. computations and the validity of the proposed model was ensured.

2.2. Material and stub column tests

The material properties of all rectangular and circular hollow sections were characterized by means of classical tensile tests. Series of coupons were extracted from the middle of two opposite flat faces – not containing the weld – of the six cold-formed rectangular hollow sections, as well as from the two opposite corners, in an attempt to characterize the expected increase in strength stemming from cold-forming effects. Two tensile coupons were also extracted from each section of the six CHS. The RHS flat coupons were 270 mm long with nominal gauge width of 10 t , where t represents the thickness of the corresponding plate. The corner prismatic coupons as well as the CHS coupons were 150 mm long with coupon dimensions of 3 mm x 3 mm cut within the cross-section thickness in order to avoid creating eccentric loads while testing (see Figure 3 and Figure 4).



Figure 3: Tensile coupons extracted from – a) flat faces of cold-formed RHS sections – b) corners of cold-formed RHS sections – c) corners of hot-rolled CHS

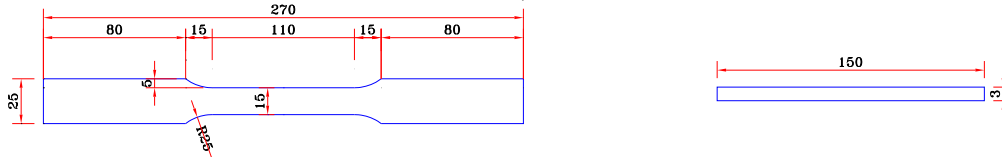


Figure 4: Typical dimensions of tensile coupons (dimensions in mm)

A 100 kN testing machine with hydraulic grips was used to test the necked coupons. The corner and CHS coupons were tested in a smaller 10 kN testing machine due to their smaller size and cross-section. The coupons were placed in the testing rig and a calibrated extensometer of 20 mm was mounted at the middle of each coupon. Tensile load was applied by a constant rate of strain (0.045 % / s) until fracture. In total, 36 coupon tests have been performed.

Figure 5 proposes representative examples of stress-strain curves obtained for the hot-rolled section CHS 159x5 and the cold-formed section RHS 220x120x6. As expected, hot-rolled sections exhibit classic stress-strain behavior, with distinct yield plateau and strain hardening effects. The finally-kept yield stress value f_y was taken as the average of the yield plateau stress for hot-rolled sections; 0.2 % proof stress was used as a convenient equivalent yield stress for cold-formed sections where the material response showed a pronounced non-linear behavior. The Young's modulus E was taken as the gradient between 20% and 80% of f_y in the elastic part using a linear regression analysis.

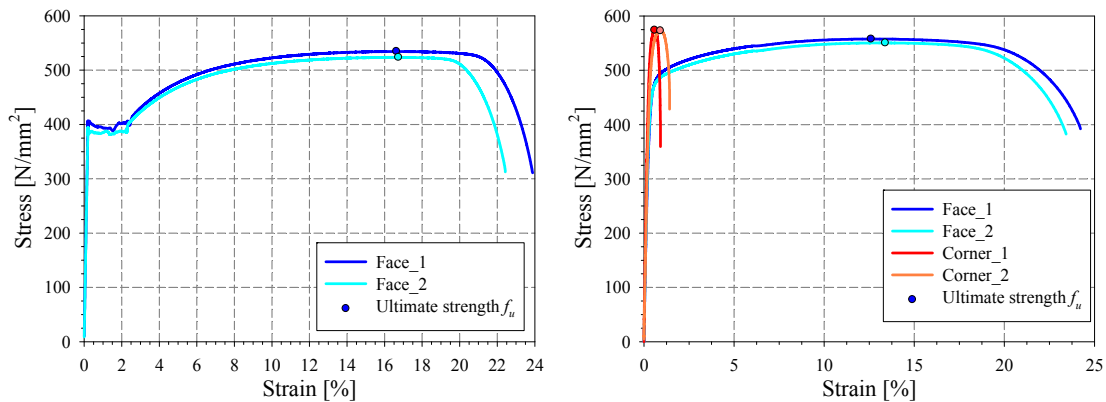


Figure 5: Typical example of engineering stress-strain curves for – a) hot-rolled CHS 159x5 – b) cold-formed RHS 220x120x6

Resistance results are presented in Table 2 where E_m represents the mean value of the measured section Young's modulus while (f_{ym}, f_{um}, f_{im}) represent the mean values of yield, ultimate and fracture stresses along with the corresponding average values of elongation ($\epsilon_{ym}, \epsilon_{um}$ and ϵ_{im}), respectively.

Table 2: Measured material properties

Section	Position of coupon	E_m	f_{ym}	ϵ_{ym}	f_{um}	ϵ_{um}	f_{tm}	ϵ_{tm}
		(kN/mm^2)	(N/mm^2)	(%)	(N/mm^2)	(%)	(N/mm^2)	(%)
RHS 200x100x4	Flat	233.1	475	0.203	583	15.7	434	27.7
	Corner	207.9	593	0.285	625	1.5	385	3.53
RHS 200x100x4	Flat	193.8	450	0.335	566	13.3	410	23.2
	Corner	217.1	573	0.266	611	1.3	361	2.67
RHS 200x100x4	Flat	206.4	480	0.234	589	12	421	21.1
	Corner	180.3	588	0.329	618	2.4	406	4.21
RHS 220x120x6	Flat	184.0	450	0.245	542	14.6	389	25.9
	Corner	205.1	590	0.288	641	1.4	438	2.81
RHS 220x120x6	Flat	182.6	462	0.253	554	13	387	23.8
	Corner	188.8	553	0.298	574	0.8	394	1.17
RHS 220x120x6	Flat	196.1	448	0.229	553	14.6	395	26.1
	Corner	183.2	585	0.32	624	1.5	355	3.33
CHS 159x5	Flat	205.0	399	0.195	543	16.3	316	23.6
CHS 159x5	Flat	198.5	393	0.198	529	16.7	312	23.2
CHS 159x5	Flat	202.2	405	0.201	537	16.2	320	23.4
CHS 159x6.3	Flat	198.9	396	0.199	539	16.4	324	22.5
CHS 159x6.3	Flat	202.7	389	0.192	522	16.1	321	21.5
CHS 159x6.3	Flat	206.4	394	0.191	529	14.9	325	19.9

Twelve compression tests were performed on stub columns extracted from all different cross-section shapes. The length of the tested specimens was chosen equal to three times the largest cross-sectional dimension, based on the principle that the length is sufficiently small to prevent member buckling while long enough to avoid an important influence of the boundary conditions and leave the development of buckling waves free. The specimens were set in a 5000 kN hydraulic machine to apply compressive axial force to the stub column specimens. Four transducers were positioned on the stub ends to measure the axial shortening of the specimens, and two strain gauges were attached at the mid-length of the specimen's adjacent plates. The attached strain gauges provided the load displacement behavior of the specimen in the elastic range in order to assess the (indirect) corresponding Young's modulus. Figure 6 shows an example of a stub column during testing.

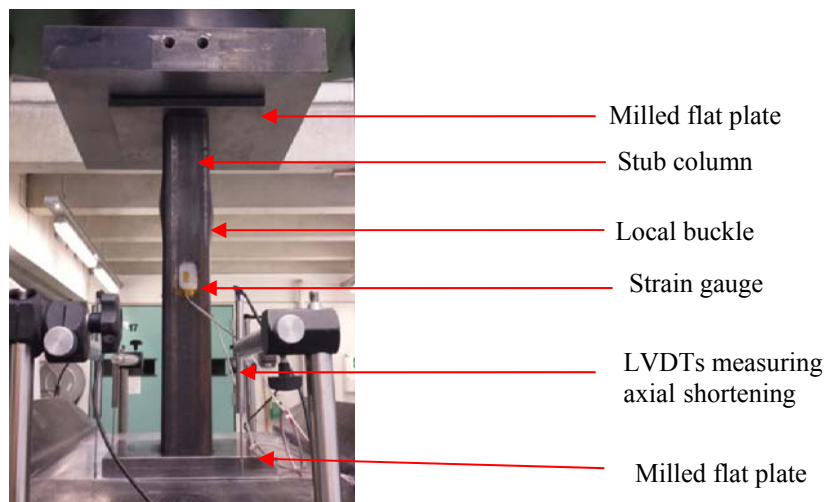


Figure 6: General stub-column test setup

Table 3 reports the obtained stub column failure loads and also allows to compare the maximum capacity obtained during the tests (i.e. with actual data $N_{pl, actual}$) and with the nominal expected load $N_{pl, nominal}$.

Table 3: Stub column test results

Specimen	Length	Weight	Calculated area	$N_{pl, actual}$	$N_{pl, nominal}$	N_{exp}	$N_{exp} / N_{pl, actual}$	$N_{exp} / N_{pl, nominal}$
	(mm)	(Kg)	(mm ²)	(kN)	(kN)	(kN)	(-)	(-)
RHS Stub CF 200x100x4	603	10.4	2197	1044	780	770	0.74	0.99
RHS Stub CF 200x100x4	601	10.4	2204	992	783	765	0.77	0.98
RHS Stub CF 200x100x4	598	10.3 5	2205	1058	783	775	0.73	0.99
RHS Stub CF 220x120x6	660	19.15	3696	1663	1312	1608	0.97	1.23
RHS Stub CF 220x120x6	657	19.05	3694	1705	1311	1622	0.95	1.24
RHS Stub CF 220x120x6	659	19.1	3692	1652	1311	1611	0.98	1.23
CHS Stub HR 159x5	475	10	2682	1070	952	1233	1.15	1.29
CHS Stub HR 159x5	478	10	2665	1047	946	1220	1.16	1.29
CHS Stub HR 159x5	475	9.95	2668	1082	947	1162	1.07	1.23
CHS Stub HR 159x6.3	474	11.65	3131	1240	1111	1481	1.19	1.33
CHS Stub HR 159x6.3	474	11.41	3066	1191	1089	1437	1.21	1.32
CHS Stub HR 159x6.3	476	11.5	3078	1211	1093	1470	1.21	1.35

2.3. Residual stresses

Basically, the sectioning technique was used to measure residual stresses, from the deformations experienced by strips cut all along the sections. Measurements were also taken with electrical strain gauges and compared to the ones obtained by the mechanical procedure.

Released residual stresses were first measured by mechanical means. The specimens were divided into strips of 150 mm length and 30 mm width and labeled. Prior to cutting, each strip length was measured by an extensometer with an accuracy of $\pm 3 \mu m$ whilst the curvature reference was measured by means of a curvature dial. Cutting of the strips was then performed on an automated milling machine followed by additional measurements of lengths and curvatures of the released strips. The differences between initial and final strips length are linked to membrane stresses, while the curvature variations are due to flexural – through thickness – stresses (see Figure 7). For both initial and final readings, a mean value was determined from five consecutive readings.

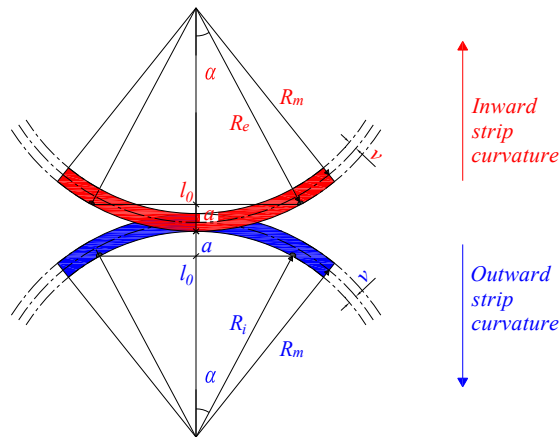


Figure 7: Geometrical deformation due to residual stresses (membrane and flexural)

After recording all initial lengths and curvatures, a series of strain gauges were glued to the external surface of each strip in the longitudinal direction, followed by initial electrical readings. The strips were then cut and final readings were taken. The total residual stresses measured from the outer surfaces combined both bending and membrane stresses. Consequently, the membrane residual stresses were obtained by subtracting the bending stresses determined mechanically from the curvature dial, and compared to values obtained with the extensometer. Patterns of through-thickness residual stresses variations for both the electrical and the mechanical readings are presented in Figure 8 for the RHS CF 220x120x6 specimen. One may note that the bending stresses were dominant while the membrane stresses were relatively low, as typically recorded for cold-formed tubes.

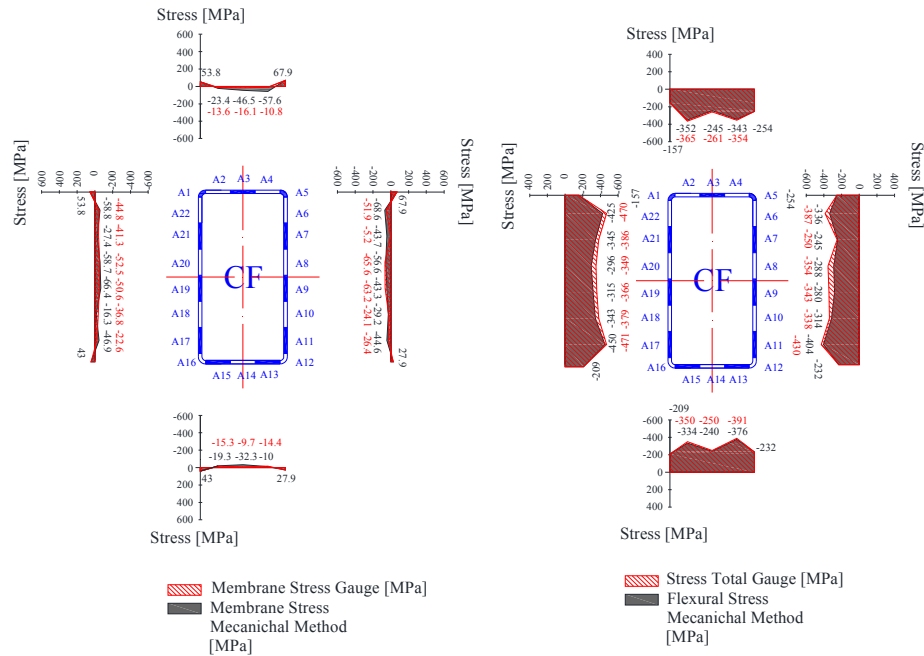


Figure 8: Mechanical and electrical measured stresses – a) membrane (right column) – b) flexural/total (left column) stresses of RHS CF 220x120x6

2.4. Geometrical imperfections

The measurement of initial imperfections was performed by means of two different procedures. The first method was based on the recordings of a set of equally spaced linear variable displacement transducers (LVDTs), used to measure the imperfections using an aluminum frame comprising a sideways-movable aluminum bar drilled at 10 equally-spaced locations (Figure 9) – some 10 vertical displacements LVDTs were used, spaced at 10 cm intervals (yellow arrow in Figure 9). In order to record data over the complete specimen, the frame was moved along the beam's length (see green arrow in Figure 9).

All transducer readings were taken simultaneously as the frame travelled along the length of the specimen – measurements were not dynamic, though. Different beam segments were measured separately with an overlapping length purposely considered to ensure the accuracy of the measurements. Three different transversal displacements were recorded for each plate.

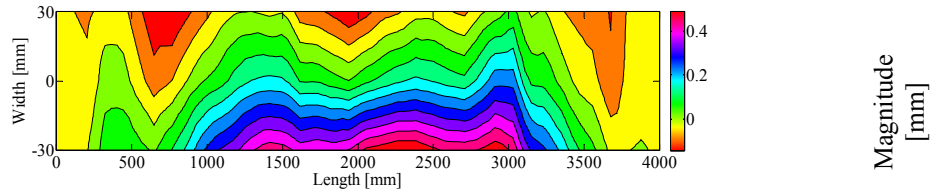
A flat, perfectly plane reference beam that have been specially manufactured in order to be considered perfectly horizontal, was used to reset the LVDTs to zero at the beginning of each set of measurements.



Figure 9: Initial geometrical imperfections measuring procedure

Figure 10 represents the corresponding out-of-flatness isolines of imperfection magnitudes obtained for some of the considered plates separately.

Bottom flange:



Left web:

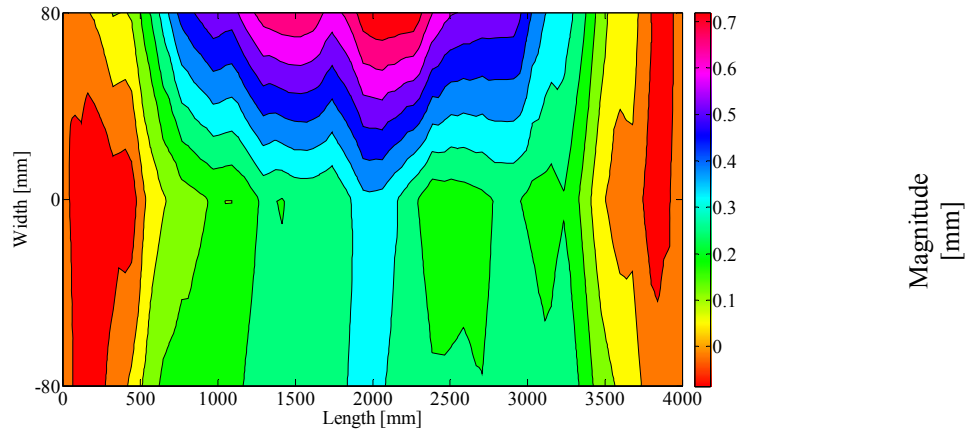


Figure 10: Measured out-of-flatness isolines of imperfection magnitudes obtained for each plate of the RHS CF 200x100x4 T2 specimen.

Before each test, the initial geometrical imperfections were also measured for the six cold-formed RHS by means of a laser Tracker *AT401* with an estimated overall accuracy of $\pm 0.5 \text{ mm}$ and an improved accuracy of $\pm 0.2 \text{ mm}$ in the expected failure zone. The columns were placed horizontally and marked with a series of targets; marks were more densely distributed at the expected location of local buckling. The principle of the measurement consists in moving a light source along predefined longitudinal lines for each plate, and recording consecutive positions (very accurately). The "tracker" technology allows the instrument to detect the reflector as illustrated in Figure 11. The remote measurements were then treated by a specific software (SA "Spatial Analyzer" of New River Kinematics) associated to the measuring instrument.

Figure 12 reports on the measured initial imperfections along the length of the RHS CF 200x100x4 T2 specimen at the mid-width of the bottom flange and left web plates, by using the LVDT and the laser tracker procedures. One may notice that there was some extra initial deformation induced into the specimen near the end plates, caused by the welding of the plates.

Laser Tracker AT401 detecting the movement of the reflector



Reflector moving along the column length

Columns placed horizontally and marked

Figure 11: Measurement of geometrical imperfections – Topometric procedure

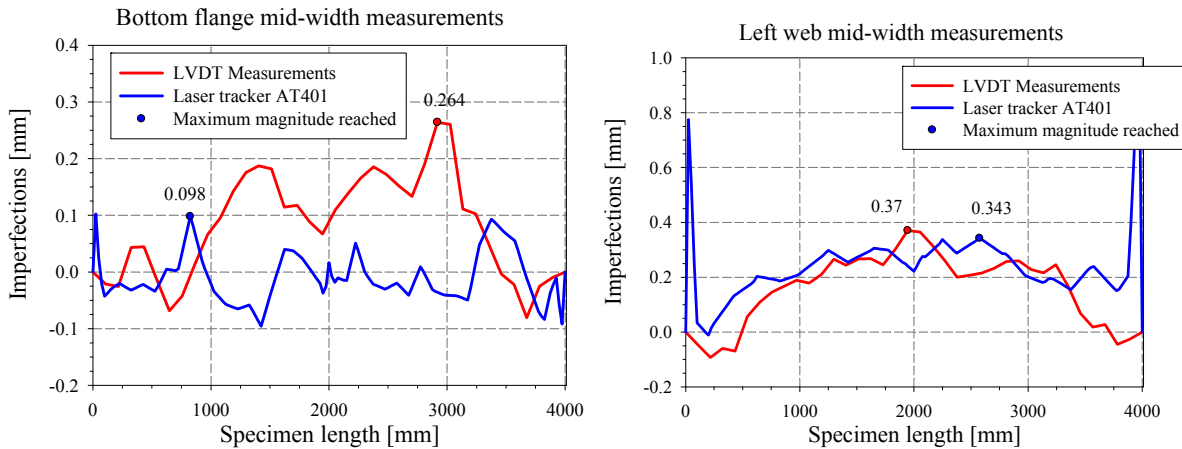


Figure 12: Initial deformations along the length of the RHS CF 200x100x4 T2 specimen at the mid-width of each plate obtained by using the LVDT and the laser tracker procedures.

Disparities in measurements are credited to the insufficient accuracy of the LVDT method. The LVDTs procedure indeed typically slightly overestimated the initial defaults. A higher level of confidence and reliability are provided by the laser *AT401* measurements. Both sets of measured initial imperfections were introduced in suitably-built shell F.E. models, along with all measured data, and were shown to lead to nearly identical numerically-predicted failure loads, indicating that the observed differences in imperfection patterns shall be deemed acceptable and sufficient.

2.5. Beam-column tests

As previously mentioned, six hot-rolled CHS as well as six cold-formed RHS shapes were tested. The ends of the tested columns were milled flat and welded to end plates of 20 mm thickness with various eccentricities, according to the desired load case. Mono-axial and bi-axial-bending with axial compression load cases were obtained by applying eccentric compression. The bending moment distributions acting on the members were therefore linear, either constant (equal and same direction eccentricities applied at both end of the specimen) or triangular (eccentricities applied at one end of the specimen only).

The end plates were bolted to two hemispherical bearings (hinges) specially designed to provide pinned-pinned end restraints for the test specimens. Each of the two bearings contained two T-shaped grooves, which enabled adjustment of the specimen when bolted to the endplates to achieve loading at the specified eccentricities. The bolts were pre-tensioned in order to prevent uplift or detachment of the specimen endplates from the hemispherical bearings.

The general test setup is presented in Figure 13. A purposely-designed rigid frame was built to ensure sufficient bracing of the tested column. The loading rig consisted in a hydraulic jack fixed at the bottom of the column and used to generate upwards compressive force. Four load cells were located under the jacks to record the force applied.

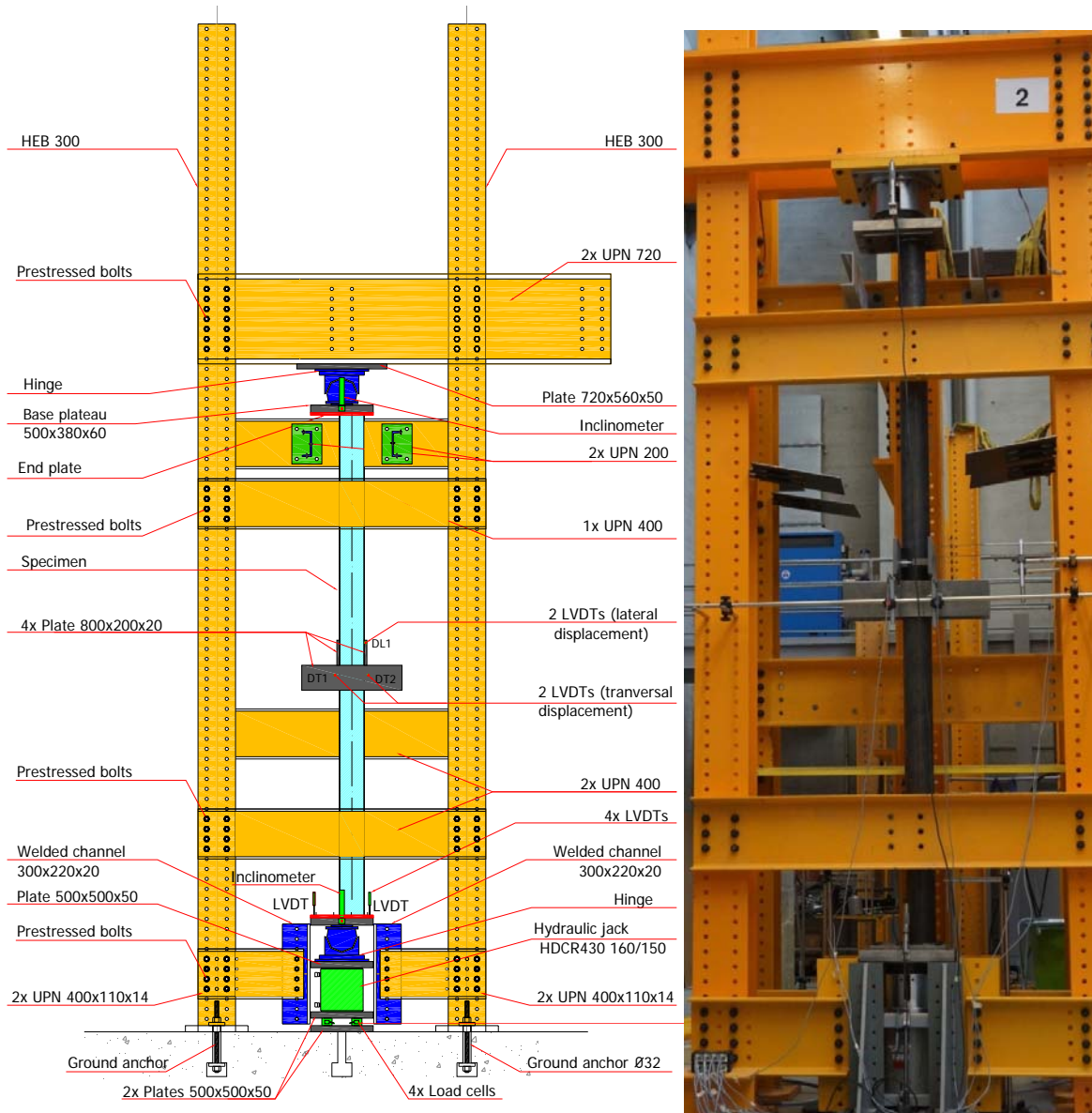


Figure 13: Overall view of test setup

Since the hydraulic jack was placed at the bottom extremity, this extremity was free to move vertically. Therefore, and in order to resist the shear forces arising when the column is tested under compression with triangular bending moment distributions, an additional supporting system aimed at resisting horizontal forces was specially designed, as illustrated in Figure 14. In one direction, these supports were formed by two triangularly-shaped pieces and anchored by threaded bolts to a base plate of dimensions 700x500x50 at each side of the specimen. In the other direction, the supports were made with welded channels 300x220x20 connected at each side of the specimen.

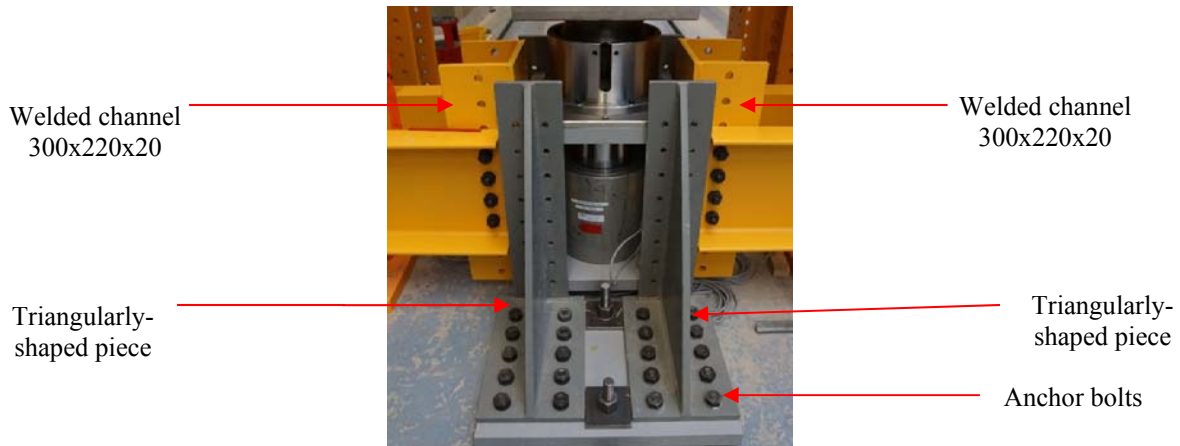


Figure 14: Embedded support designed to resist shear forces

Various transducers were used to monitor the member's response:

- 4 load cells were located under the jacks to record the applied force;
- Inclinometers were fixed at both ends of the column to measure the column end rotations in both principal bending planes;
- 4 linear variable displacement transducers were positioned on the mid-span cross-section, to measure lateral and transversal displacements by means of two independent systems (Figure 15);
- 4 linear variable displacement transducers were positioned on the bottom end plate of the specimen to record the axial shortening and rotations during testing (see Figure 16).

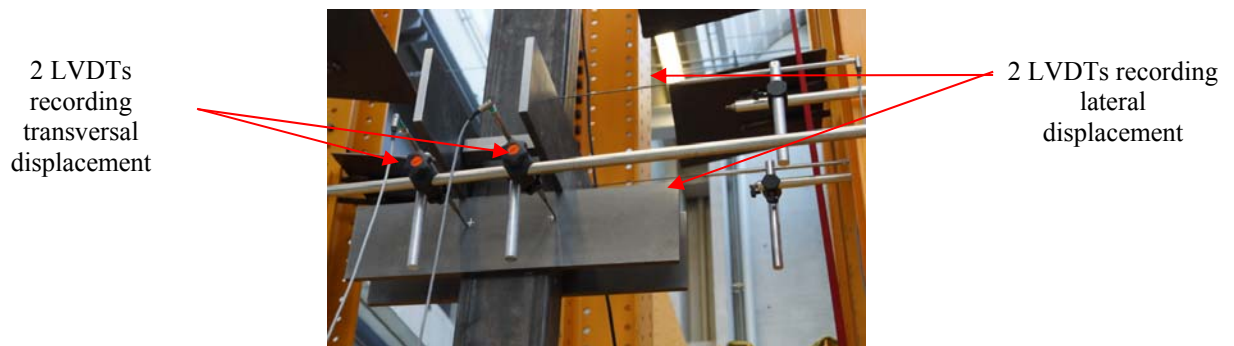


Figure 15 : Measurement of displacements in mid-span cross-section

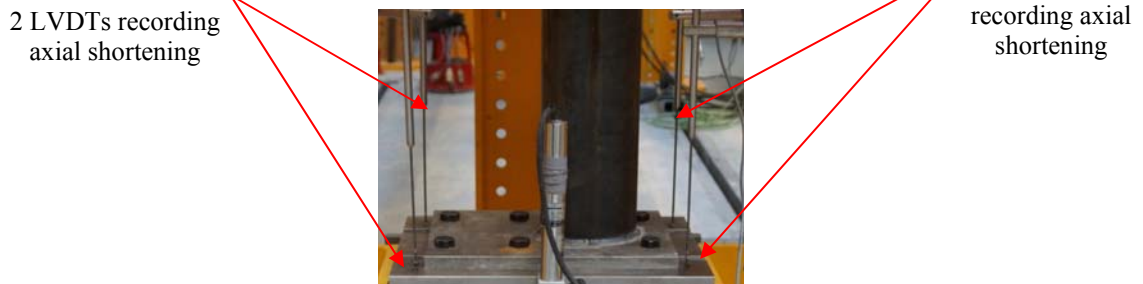


Figure 16: Measurement of axial shortening

All twelve columns were tested up to and beyond failure and all readings were taken using an electronic data acquisition system recording at a 2 Hz pace. The measured eccentricities and maximum forces of all tested specimens are listed in Table 4. Figure 17 illustrates the displacements measured by the four bottom LVDTs as well as the corresponding average displacement for the specimen CHS HR 159x6.3 T11.

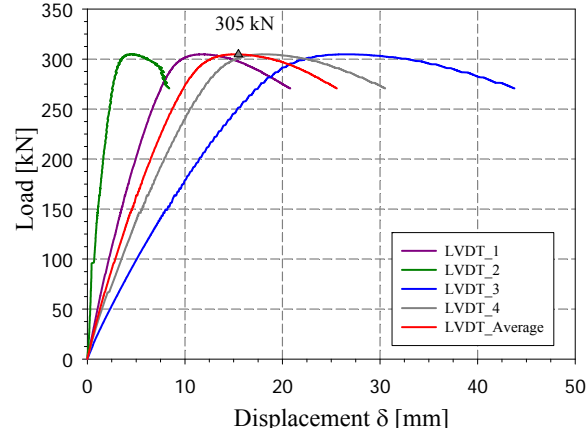


Figure 17 : Typical axial shortening curves (CHS HR 159x6.3 T11)

Table 4: Measured dimensions and experimental ultimate loads for all tested specimens

Cross-section shape	ψ (-)	Measured dimensions			F_{TEST} (kN)
		Length (mm)	e_z (mm)	e_y (mm)	
RHS CF 200x100x4 T1	1	4001.22	84.6	0	351.9
RHS CF 200x100x4 T2	1	3999.61	88.9	41.6	213.5
RHS CF 200x100x4 T3	0	4000.30	141.0	0	365.1
RHS CF 220x120x6 T4	1	4000.09	72.2	0	700.0
RHS CF 220x120x6 T5	1	4000.33	85.4	43.8	478.2
RHS CF 220x120x6 T6	0	3998.58	120.3	0	691.4
CHS HR 159x5 T7	1	3999.70	68.9	0	345.4
CHS HR 159x5 T8	1	4895.00	77.5	0	288.5
CHS HR 159x5 T9	0	4000.05	130.0	0	317.8
CHS HR 159x6.3 T10	1	4900.05	78.5	0	319.6
CHS HR 159x6.3 T11	1	4000.10	88.4	58.7	304.7
CHS HR 159x6.3 T12	0	4000.00	130.0	0	363.0

2.6. Additional experimental references

Additional well-documented similar test data from European project “Semi-Comp” (Semi-Comp 2007) have been added to the present results; this project consisted in determining the influence of semi-compact class 3 sections on member buckling behavior. The test program comprised beam-column member buckling tests on 3.5 m to 4.5 m length profiles with hot-rolled H-shaped as well as cold-formed tubular cross-sections. The columns were tested under mono-axial or biaxial bending with axial compression. Linear bending moment diagrams were selected for each test as summarized in Table 5 for the tubular sections, where ψ_y and ψ_z represent the ratios between end moment about y - y and z - z axes, respectively. The member buckling tests eccentricities adopted are presented in Table 5 as well. The combined load cases were obtained through an eccentric load applied at the ends of the specimens through welded thick end plates. The support conditions of the members during the tests may be assumed to be “pinned

conditions”: the end sections bending rotations can be assumed to be free. The full test program can be found in (Semi-Comp 2007).

Table 5: “Semi-Comp” test program for member buckling

RHS 200x120x4 (S275) $L = 4 m$	ψ_y	ψ_z	e_y	e_z	SHS 180x5 (S355) $L = 4 m$	ψ_y	ψ_z	e_y	e_z
	(-)	(-)	(mm)	(mm)		(-)	(-)	(mm)	(mm)
R275 BU 1	1	/	55	0	S355 BU 1	1	/	55	0
R275 BU 2	0	/	55	0	S355 BU 2	0	/	55	0
R275 BU 3	/	1	0	45	S355 BU 3	-0.455	/	55	0
R275 BU 4	/	0	0	45	S355 BU 4	1	1	55	55
R275 BU 5	1	1	55	45	S355 BU 5	0	0	55	55
R275 BU 6	0	0	55	45	S355 BU 6	-0.455	-0.5	55	55

Besides the main member buckling tests, the material properties, residual stresses and initial geometrical imperfections were determined and incorporated in the numerical model in order to achieve the validation in the most rigorous way. Accordingly, tensile coupon tests were extracted from the flat faces and the corners (where an increase of f_y is expected) of the tubular profiles for each type of cross-section. Concerning the measurement of residual stresses, the cutting strip technique had been used. A rather low level of membrane stresses was observed compared to the level of flexural stresses for the cold-formed tubular profiles. The initial geometrical imperfections were also measured since it has an influence on the carrying capacity of the members.

3. Development and validation of F.E. models – Parametric studies

3.1. Shell F.E. models

Series of numerical computations have been led with the use of non-linear F.E.M. FINELg, continuously developed at the University of Liège and Greisch Engineering Office since 1970 (Greish and ULg, FINELg 1999). This software offers almost all types of F.E.M. analyses, and present investigations have mainly been resorting to so-called M.N.A. (Materially Non-linear Analysis), L.B.A. (Local Buckling Analysis) and G.M.N.I.A. (Geometrically and Materially Nonlinear Analysis with Imperfections). The cross-sections were modelled with the use of quadrangular 4-nodes plate-shell finite elements with typical features (Corotational Total Lagrangian formulation, Kirchhoff’s theory for bending). The corners of square and rectangular profiles were modeled with two shell elements per corner.

In order to adopt the most appropriate meshing density, able to provide an accurate numerical prediction of the member’s behavior, a series of preliminary GMNIA F.E. calculations were performed on different sizes of SHS and RHS of nominal steel grade S355. Two different element lengths: $L = 1500 mm$ and $L = 3000 mm$ were considered as well as two different loading conditions: pure compression and major-axis bending with a constant moment distribution along the member. Different types of mesh densities were tested as shown in Figure 18, where the selected meshing types ranged from fine (*Type I* meshing) to coarse (*Type IV* meshing).

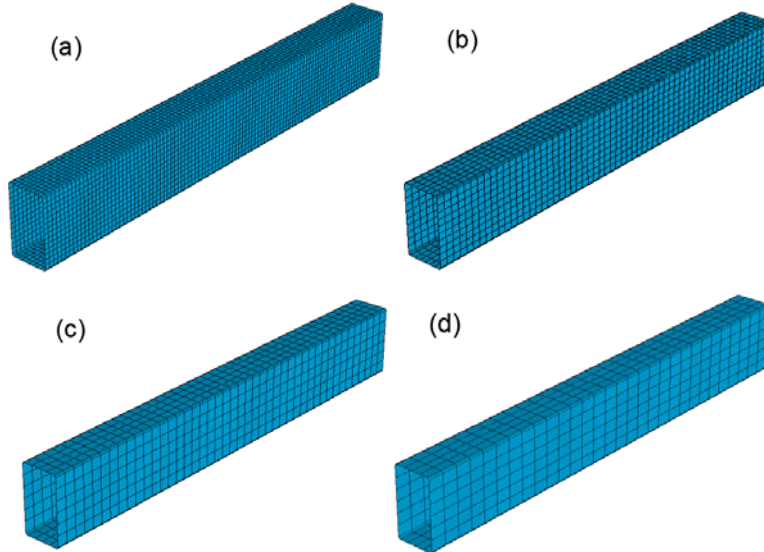


Figure 18: Mesh density study for rectangular sections – a) *Type I* – b) *Type II* – c) *Type III* – d) *Type IV*

For sake of simplicity and clarity, only results concerning the RHS of $L = 3000 \text{ mm}$ are presented in Figure 19. One directly observes that coarse meshes (*Type III* and *Type IV*) do not lead to acceptable results, being by as much as 13 % lower than those of *Type I* mesh in the worst cases; therefore, these meshes have not been considered further. Reasonable results and negligible differences are however observed for denser meshes (*Type I* and *Type II*), for all sections and load cases. Accordingly, mesh *Type II* was selected as it leads to satisfactory results with minimal computational effort.

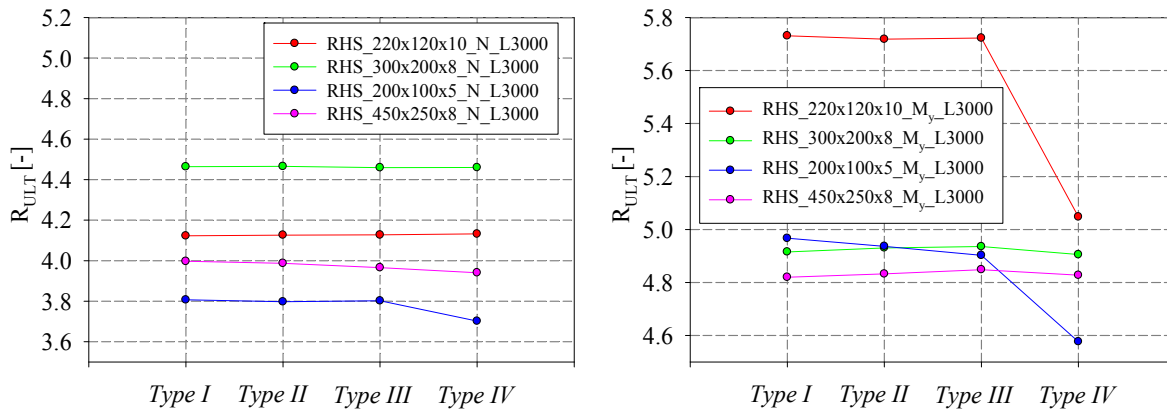


Figure 19: Mesh density studies – Results for RHS sections

3.2. Assessment towards own buckling tests

A numerical model was developed so as to represent accurately the experimental behavior of the tested columns. End plates were modeled through rigid plates having an equivalent thickness of 80 mm (which is equal to the width of the hinge connecting plate and the specimen's end plate together), with shell elements that remained elastic during loading. The plates' stiffness allowed an even distribution of the applied load at the ends of the sections and prevented the cross-sectional deformation at both ends. Truss elements were used to simulate the (assumed) rigid spherical hinges at both ends, and allowing free rotations. All trusses were connected to the end plates nodes and to the centroid of the hinge (see Figure 20). The load was applied at the centroid

of the hinge, and the cases of combined bending with compression were simulated through an axial load applied at the centroid of the hinge with the corresponding measured eccentricities (Nseir J. 2015). It may be noted here that the buckling length (which corresponds to the distance between the centers of the spherical hinges) was respected in the numerical models as well.

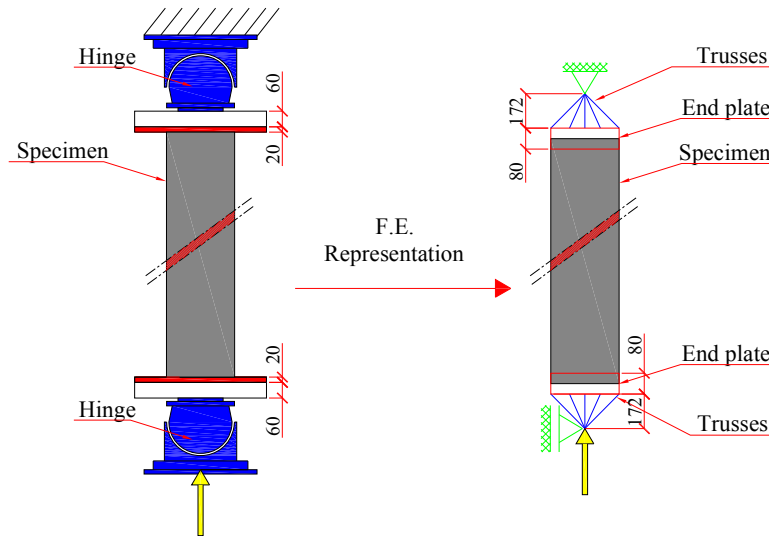


Figure 20: Finite element model assumptions

Every measured data was considered and taken into account for the validation of the F.E. models. In particular, the actual dimensions (section geometry and length) and material behavior of the tested specimens were introduced in the F.E. models, as well as the measured geometrical imperfections. Since the membrane residual stresses are insignificant in the cold-formed sections, flexural stresses were only considered. As for the circular hot-rolled profiles, only flexural residual stresses were introduced.

Averaged measured material stress-strain behavior including strain-hardening effects was also included. An elastic-perfectly plastic with 2% strain hardening material law was implemented for hot-rolled profiles. Regarding the cold-formed tubular profiles, two material laws have been defined: one for the base material and one for the corner regions. A simple Ramberg-Osgood material law was used for the flat regions and a multi-linear law was adopted for the corners region as illustrated in Figure 21.

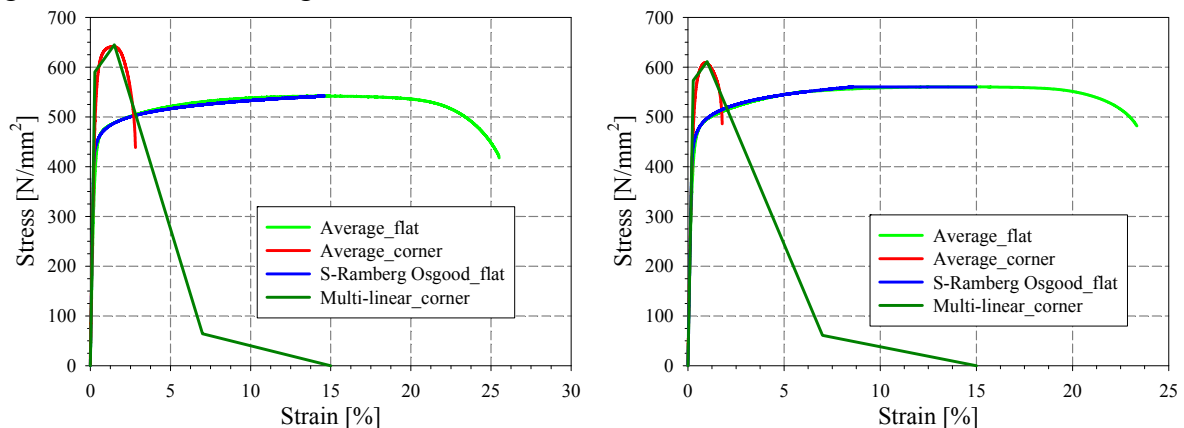


Figure 21: Material stress-strain laws adopted in F.E. calculations for specimens – a) RHS CF 220x120x6 T4 – b) RHS CF 200x100x4 T2

A simple Ramberg-Osgood law was shown to be inadequate to represent the corners' region (Nseir J. 2015), since this material law is characterized by a limited ductility and a maximum strain of 2.5 %. Therefore, once the section reached that level of strain, the corners would find themselves ineffective leading to the failure of the entire section and no more strains could be achieved beyond this value of 2.5% strain. However, owing to numerical needs in ductility, the specific pattern of Figure 21 was adopted, with negative stiffness allowing a reduced participation of the corners to the resistance beyond 2.5% strain.

Table 6 provides the numerical ultimate loads obtained in considering initial imperfections by means of equally spaced LVDTs, the experimental ultimate loads and the ratio of the experimental ultimate loads to their numerical counterparts for all investigated columns. It can be observed that the numerical models accurately predicted the ultimate carrying capacities and represented the beam-column's response conveniently, whatever the cross-section, loading arrangement, length... Mean and standard deviation values further highlight the accuracy and consistency of the numerical model which provides excellent accordance with the test results in terms of ultimate loads.

A graphical comparison of the ultimate loads obtained numerically by using the initial imperfections measured by means of the LVDTs and the experiments is shown in Figure 22 for all tested specimens. The red lines presented in the graphical comparisons indicate a deviation of +/- 10 % from equality. It can be seen that all numerical simulations give good predictions of the ultimate loads of loaded columns; all values oscillate very closely around the $F_{TEST} / F_{F.E.M.} = 1.0$ ideal line.

It should also be noted that the numerical models are seen to sometimes provide slightly unsafe results, however not more than 4 % on the unsafe side. This may be due to experimental uncertainties that exist during the preliminary measurement processes.

Table 6: Comparison of numerical and experimental ultimate loads

Cross-section shape	Load case	ψ	L	e_z	e_y	F_{TEST}	F_{FE_LVDT}	F_{TEST}/F_{FE_LVDT}
		(-)	(mm)	(mm)	(mm)	(Kn)	(kN)	(-)
RHS CF 200x100x4 T1	60%N+40%M _y	1	4001.2	84.6	0	352	348	1.01
RHS CF 200x100x4 T2	40%N+30% M _y +30%M _z	1	3999.6	88.9	41.6	214	219	0.98
RHS CF 200x100x4 T3	60%N+40%M _y	0	4000.3	141.0	0	365	336	1.09
RHS CF 220x120x6 T4	60%N+40%M _y	1	4000.1	72.2	0	700	669	1.05
RHS CF 220x120x6 T5	40%N+30%M _y +30%M _z	1	4000.3	85.4	43.8	478	448	1.07
RHS CF 220x120x6 T6	60%N+40%M _y	0	3998.6	120.3	0	691	670	1.03
CHS HR 159x5 T7	50%N+50%M _y	1	3999.7	68.9	0	345	308	1.12
CHS HR 159x5 T8	50%N+50%M _y	1	4895.0	77.5	0	289	267	1.08
CHS HR 159x5 T9	50%N+50%M _y	0	4000.0	130.0	0	318	306	1.04
CHS HR 159x6.3 T10	50%N+50%M _y	1	4900.0	78.5	0	320	332	0.96
CHS HR 159x6.3 T11	33%N+33%M _y +33%M _z	1	4000.1	88.4	58.7	305	313	0.97
CHS HR 159x6.3 T12	50%N+50%M _y	0	4000.0	130.0	0	363	366	0.99
Mean								1.03
Standard deviation								0.05

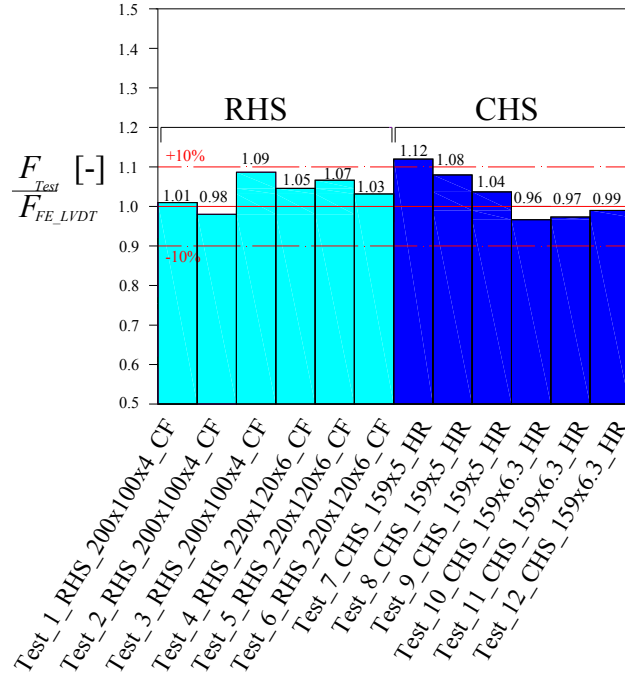


Figure 22: F.E. peak loads vs. experimental loads.

Figure 23 gives examples of experimental and numerical axial load-displacement curves. It can be seen that all numerical simulations provide excellent accordance with the test results in terms of ultimate loads, displacements, initial stiffness, failure modes...

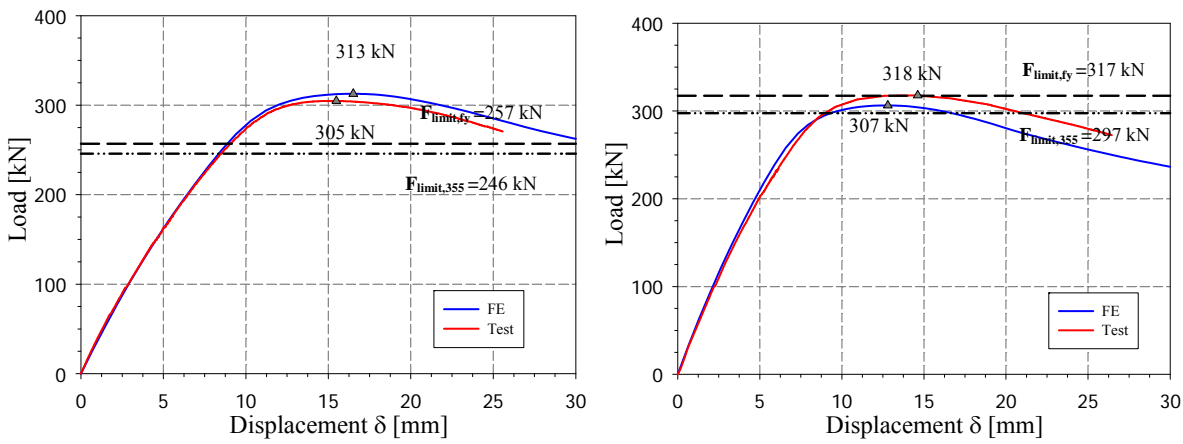


Figure 23: Numerical vs. experimental axial load displacement curves of specimens – a) CHS HR 159x6.3 T11 – b) CHS HR 159x5 T9

3.3. Assessment towards additional test results

A similar F.E. model has been developed so as to fit as closely as possible with the corresponding test arrangements of the second test series used herein (Semi-Comp 2007). Pinned-end conditions were applied and additional rigid end plates, modeled with shell elements with an elastic material law and linked to the specimen on both sides. The load was applied through nodal forces at the middle of the endplates, similarly to the test conditions. The thick plates allowed an even distribution of the applied load with no out-of-plane deformations.

Mesh *Type II* was again selected. Every measured data was taken into account for the validation of the F.E. models as closely as possible to the experimental conditions. Measured dimensions as well as measured material properties were introduced to the numerical model.

Averaged material stress-strain behavior including strain hardening effects was used. Two material laws have been defined: one for the flat regions where a simple Ramberg-Osgood material law was used, and one for the corner regions where a multi-linear law was adopted.

The adopted membrane residual stresses pattern for the numerical validation has been taken as an approximation of the measured residual stresses with respect to an auto-equilibrated pattern. The measured initial geometrical imperfections were also introduced.

The twelve beam-column tests performed at the laboratory of the University of Liège were modeled using FINELg F.E. software. The predicted ultimate loads were compared to the experimental ones and are presented in Table 7 for each beam-column test, where the agreement between the finite element predictions and its experimental counterpart seen to be very good for all considered cases. Figure 24 shows a graphical comparison of the ultimate loads from F.E. results with the experimental results. Figure 25 gives typical examples of experimental and numerical axial load-displacement curves.

Table 7: Comparison of numerical and experimental ultimate loads from “Semi-Comp” project (Semi-Comp 2007).

Test #	Specimen	Section	L	F_{TEST}	F_{FE}	F_{TEST}/F_{FE}
			(mm)	(kN)	(kN)	(-)
1	S355 BU 1	SHS S355CF 180x180x5	4050	563	580	0.97
2	S355 BU 2	SHS S355CF 180x180x5	4050	656	698	0.94
3	S355 BU 3	SHS S355CF 180x180x5	4050	708	747	0.95
4	S355 BU 4	SHS S355CF 180x180x5	3990	460	483	0.95
5	S355 BU 5	SHS S355CF 180x180x5	4050	600	605	0.99
6	S355 BU 6	SHS S355CF 180x180x5	4020	629	643	0.98
7	R275 BU 1	RHS S275CF 200x120x4	4050	404	394	1.03
8	R275 BU 2	RHS S275CF 200x120x4	4050	451	465	0.97
9	R275 BU 3	RHS S275CF 200x120x4	4050	261	254	1.03
10	R275 BU 4	RHS S275CF 200x120x4	4050	331	314	1.06
11	R275 BU 5	RHS S275CF 200x120x4	4050	268	243	1.10
12	R275 BU 6	RHS S275CF 200x120x4	4050	307	301	1.02
Mean						1.00
Standard deviation						0.05

These results again show that the numerical models could accurately predict the ultimate carrying capacities and represent the beam-column’s response conveniently. The mean and standard deviation values further highlight the accuracy and consistency of the numerical model.

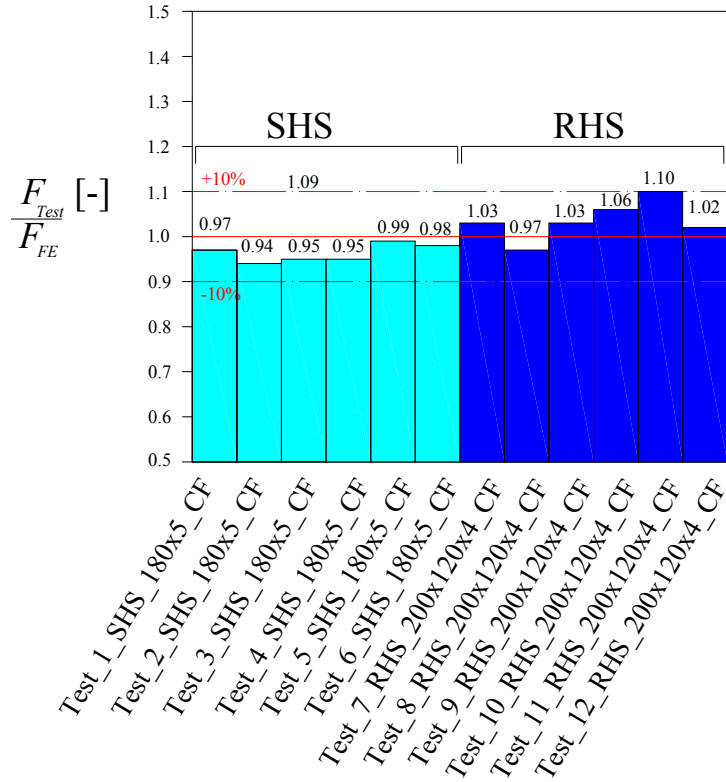


Figure 24: F.E. peak loads vs. experimental loads.

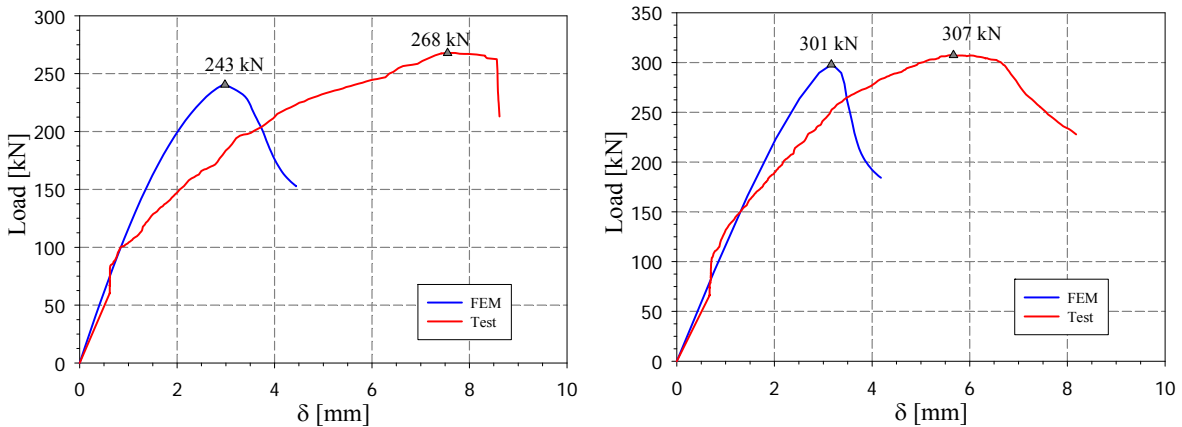


Figure 25: Numerical vs. experimental axial load displacement curves of specimens – a) R275_BU_5– b) R275_BU_6

3.4. F.E. parametric studies

The finite element model was further used to generate an extensive set of numerical beam-column “virtual” tests to investigate deeply the structural behavior of members tested under simple and combined loadings. The numerical study covered both hot-rolled and cold-formed sections and aimed at characterizing their physical behavior with respect to many influences. Adequate parameters were chosen in order to cover different section shapes belonging to all classes defined according to the Eurocode 3 classification system (EN 1993-1-1 2005) and different element lengths.

A derived FE-model has been implemented on the basis of the validated one. Quadrangular four node shell elements with Corotational Total Lagrangian formulation have been adopted in all simulations. The support conditions and the introduction of applied loads received particular attention, and use of so-called kinematic linear constraints has been made to ensure a “plane-sections-remain-plane” behavior of the end sections. Following ideal simply-supported “fork” support conditions, end cross-sections can only exhibit a maximum of three degrees of freedom: axial global displacement, rotation about the strong axis and rotation about the weak axis. Only three different nodes are then necessary to describe the displacement of any point in the cross-section once the linear relationships for axial displacements are established, as a function of the displacement of the three “longitudinal-free” nodes. In other words, a maximum of three nodes may experience a “free” longitudinal displacement, all other nodes’ x-displacements linearly depending on the longitudinal displacements of the “x-free” nodes to respect a global cross-sectional displaced configuration. The three nodes were chosen at the plate edges (near different corners) of the cross-section, and all the nodes in between were constrained to the three main nodes through linear relationships. Additional fictitious nodes have been defined at the centroids of the end-cross-sections for the definition of “beam-like” support conditions, and transverse supports preventing from local buckling have also been implemented in each plate. External loading was applied through four concentrated forces at the member’s ends (i.e. strong, weak axis bending moments and axial forces) and has been implemented at the flanges’ plates as shown in Figure 26.

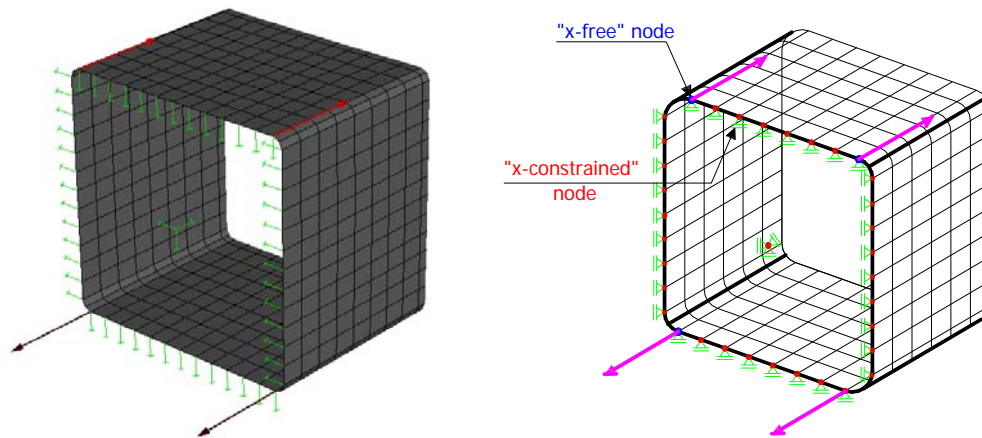


Figure 26: Loading and support conditions

The same mesh density as described previously was used in all simulations. Both global and local initial geometrical defaults were taken into account in the F.E. models. *Local* imperfections shapes were introduced through an appropriate modification of node coordinates of the considered plate (i.e. web or flange) with a combination of sine waves in both directions in square half-wave patterns. Suitable inward-outward directions have been adopted to keep certain continuity in the overall pattern (see Figure 27). The adopted sine period was equal to the average period of both constitutive plates of the section, with the most reasonable and realistic amplitude of imperfections chosen as a per plate amplitude $a / 200$ with ‘ a ’ equal to $(b - t - 2r)$ or $(h - t - 2r)$ as suggested by Nseir (Nseir J. 2016).

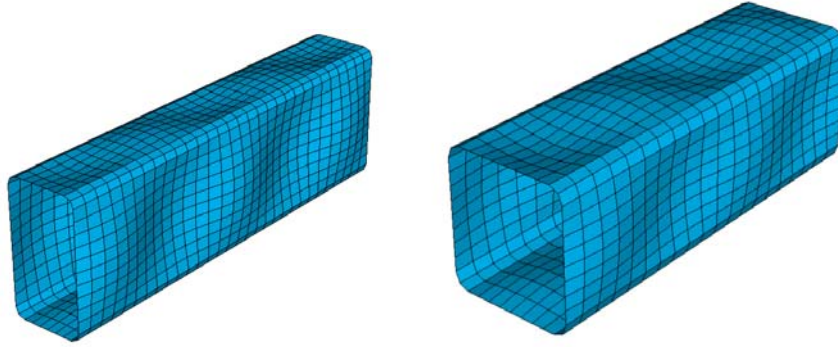


Figure 27: *Local* geometrical imperfections adopted for both square and rectangular hollow sections (magnified)

The initial *global* geometrical imperfections have been basically introduced through adequate modifications of node coordinates following sine shapes in both major and minor-axes with the realistic average value of global imperfection amplitude equal to $L / 1000$ in each principal plane as illustrated in Figure 28.

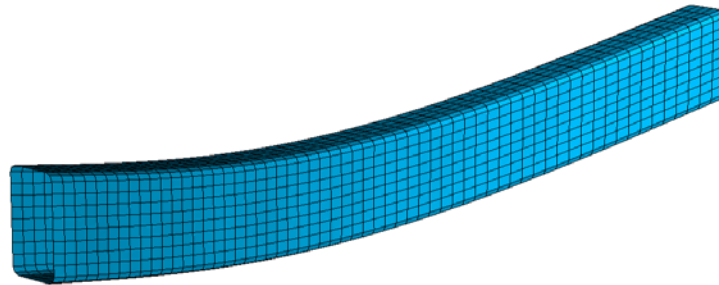


Figure 28: Magnified initial *global* geometric imperfections

Then, parametric numerical calculations have been carried out on tube members, and considered the following parameters:

- 13 different element lengths varying from 1500 *mm* to 15000 *mm* in order to represent the whole practical range of member slenderness;
- 3 different steel grades: S235, S355, S690;
- 2 fabrication processes: hot-rolled and cold-formed;
- 8 cross-section shapes: rectangular and square hollow sections covering “plastic” to “slender” responses of the sections;
- Numerical calculations were performed through both beam (i.e. where member behavior can only take into account *global* instabilities regardless of *local* buckling) and shell element models (i.e. where the member interactions curves properly accounted for local/global buckling interaction behavior);
- Different loading conditions:
 - pure compression N ;
 - compression with major-axis bending $N+M_y$;
 - compression with minor-axis bending $N+M_z$;
 - compression with biaxial bending $N+M_y+M_z$.

A distinction has been made between the different loading situations, namely with respect to:

- Linear bending moments distributions, defined as the ratio between applied end moments: 5 coefficients were adopted $\psi_y = \psi_z = -0.33$, $\psi_y = \psi_z = 0$, $\psi_y = \psi_z = 0.33$, $\psi_y = \psi_z = 0.67$, $\psi_y = \psi_z = 1.0$;
- The relative axial force ratio defined according to EN 1993-1-1 as $n = N / N_{b,Rd}$ where:

$$N_{b,Rd} = \chi N_{pl} \text{ for class 1, 2 and 3 cross-sections;}$$

$$N_{b,Rd} = \chi N_{eff} \text{ for class 4 cross-sections;}$$

$N_{b,Rd}$, N_{pl} and N_{eff} represent respectively the buckling, plastic and effective resistance of the member; χ represents the reduction factor for instability; 5 values of the relative axial force ratio n were adopted ranging from 0.15 (i.e. the load case becoming thus a compression of 15% $N_{b,Rd}$ with monoaxial or biaxial bending), to 1.0 (i.e. the load case becoming thus 100% $N_{b,Rd}$, a pure compression one);

- The degree of biaxial bending defined for combined load cases as the ratio M_y / M_z . This ratio was varied on the basis of an angle $\alpha_{baxiality}$ in order to investigate the influence of the proportion of the major and minor-axis bending on the member resistance. For each load case, 10 values of the degree of biaxial bending were adopted varying from $\alpha_{baxiality} = 0^\circ$ (i.e. the load case becoming compression with major-axis bending $N+M_y$) to $\alpha_{baxiality} = 90^\circ$ (i.e. the load case becoming compression with minor-axis bending $N+M_z$), as shown in Figure 29 for different types of cross-section classification.

Additional calculations were performed with the same parameters with a length equal to three times the height of the section in order to determine the cross-section resistance numerically.

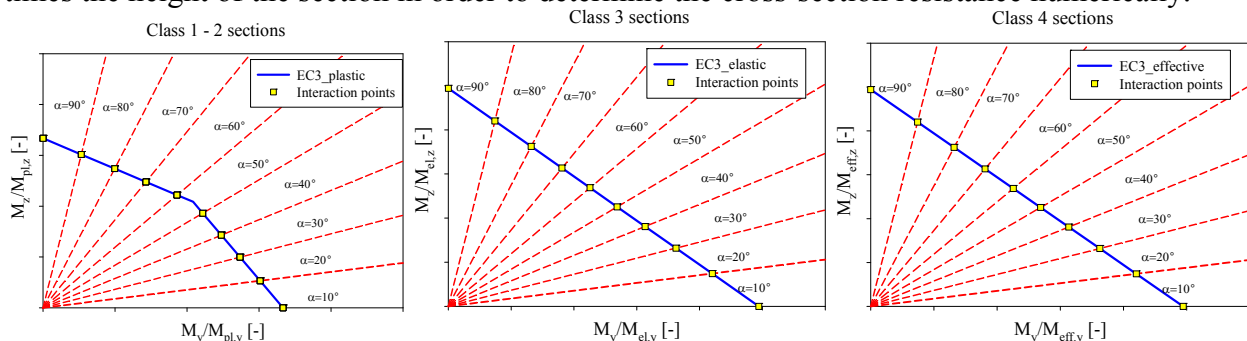


Figure 29: Selection of load cases for $N+M_y+M_z$ combined situations – a) class 1-2 – b) class 3 – c) class 4

4. Assessment of proposed design approach

4.1. O.I.C. approach for local/global coupled interactions

Figure 30 shows all gathered numerical results relative to hot-rolled and cold-formed beam-column tests, respectively, represented in an O.I.C. format.

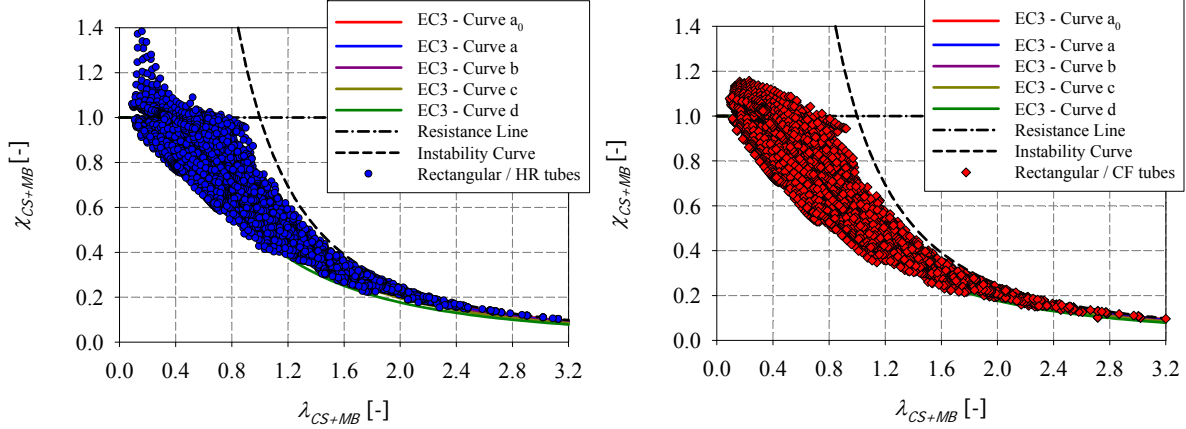


Figure 30: Numerical results for members obtained for – a) hot-rolled RHS– b) cold-formed RHS

The horizontal axis represents the generalized slenderness λ_{CS+MB} defined in Equation (1) while the vertical axis reports the member reduction factor χ_{CS+MB} defined in Equation (2):

$$\lambda_{CS+MB} = \sqrt{\frac{\chi_{CS} \cdot R_{RESIST}}{R_{STAB,MB}}} \quad (1)$$

$$\chi_{CS+MB} = \frac{R_{REAL}}{\chi_{CS} \cdot R_{RESIST}} \quad (2)$$

In Equation (1) and Equation (2), χ_{CS} represents the cross-section reduction factor behavior. In all subsequent results, χ_{CS} values have been evaluated numerically (suitable shell non-linear F.E. simulations) so as to provide a fair estimation of the influence of local buckling on the members' overall responses⁵. The final resistance factor R_{REAL} was computed using shell elements so that local and global instabilities interact; R_{REAL} is affected by resistance and instability as well as by initial imperfections (i.e. residual stresses, geometrical imperfections), by the material law, load case definition, section geometries, boundary conditions...). R_{RESIST} represents the load ratio to reach the resistance (plastic) limit and was computed using a dedicated Matlab tool developed to calculate the exact plastic capacity of the section (Epiney V. 2015); $R_{STAB,MB}$ represents the load ratio to reach the instability limit and was computed using Abaqus software with beam modelling for members (i.e. influence of cross-section instabilities is excluded).

4.2. Design proposal for HSS beam-column members

With the adoption the Ayrton-Perry format detailed in Equation (3), several factors were fitted based on the numerical results. All the reference F.E. results were analyzed and sorted to identify the key parameters to be kept for the derivation of design curves.

$$(1 - \chi)(1 - \chi\lambda^2) = \eta\chi \quad (3)$$

⁵ Analytical expressions were developed to get χ_{CS} and can be found in (Nseir J. 2015).

where χ is the reduction factor, λ is the relative slenderness and η is the factor accounting for generalized imperfections. Figure 31 shows the schematic representation of the Ayrton-Perry approach.

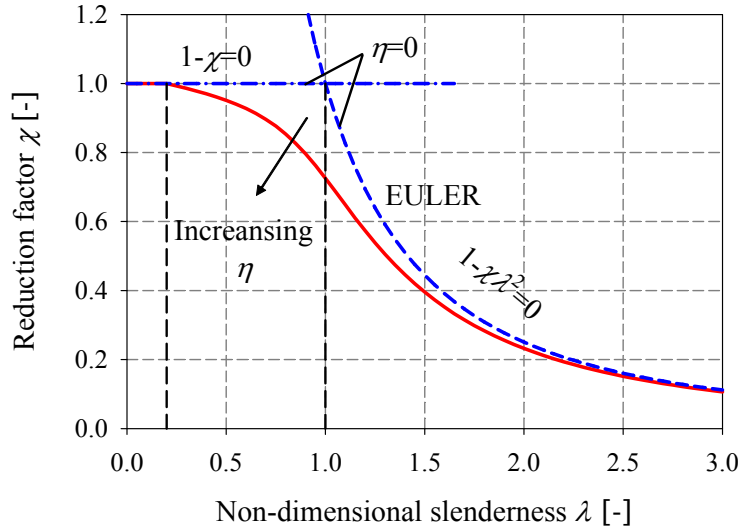


Figure 31: Schematic representation of the Ayrton-Perry approach.

Equation (3) can be rearranged in the following form:

$$\chi_{CS+MB} = \frac{1}{\phi_{CS+MB} + \sqrt{\phi_{CS+MB}^2 - \lambda_{CS+MB}^2}} \quad (4)$$

$$\text{where } \phi_{CS+MB} = 0.5(1 + \alpha(\lambda_{CS+MB} - \lambda_0) + \lambda_{CS+MB}^2) \quad (5)$$

The following factors defined below were locally determined through a best-fit procedure for simple and combined loading, for hot-rolled and cold-formed sections:

- The end of plateau λ_0 value;
- The imperfection factor α .

4.3. Columns in simple compression

The results relative to cold-formed shell members are only presented in the following for sake of clarity; identical investigations have nevertheless been led for hot-rolled H.S.S. situations as well. An additional sub study has been undertaken including sections having high yield stresses ($f_y = 460 \text{ N/mm}^2$, $f_y = 770 \text{ N/mm}^2$, $f_y = 960 \text{ N/mm}^2$) in an attempt to characterize more precisely the influence of the yield stress on the member resistance under pure compression. Obtained results are illustrated in Figure 32.

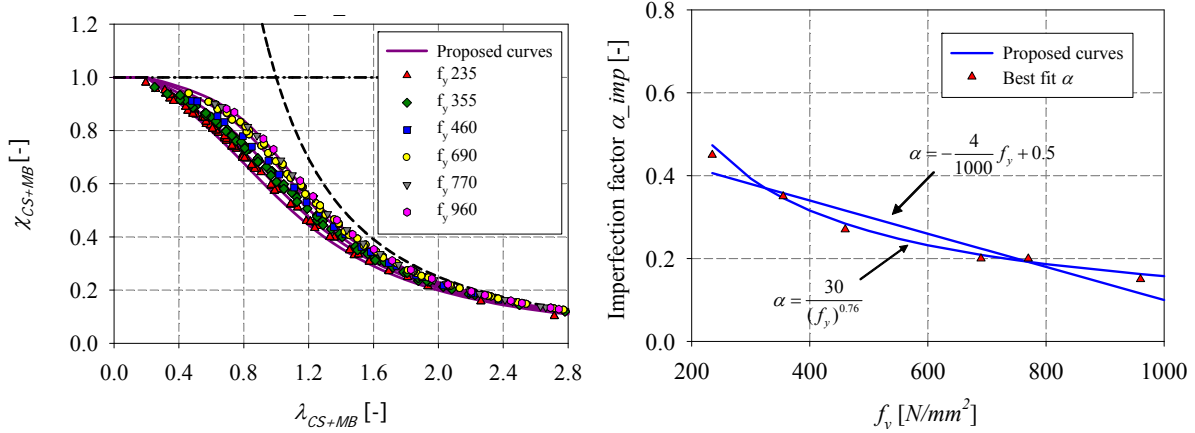


Figure 32: Application of the O.I.C. to cold-formed SHS and RHS of different steel grades under compression

According to Eurocode 3, buckling *Curve c* is adopted for cold-formed sections for the following nominal yield stresses: $f_y = 235 \text{ N/mm}^2$, $f_y = 275 \text{ N/mm}^2$, $f_y = 355 \text{ N/mm}^2$, $f_y = 420 \text{ N/mm}^2$ and $f_y = 460 \text{ N/mm}^2$. However, it is clearly seen from the numerical results that an increased yield stress leads to higher resistance curves. Therefore, the local-global buckling interaction is treated in structural design codes in a manner that is potentially too conservative for high-strength hollow sections members. Accordingly, multiple “design” χ_{CS+MB} interaction curves were derived for each cold-formed column depending on the corresponding steel grade and finally relationships were established between the imperfection factor α and the corresponding yield stress f_y (see Figure 32).

Table 8 summarizes the proposed parameters for the design curves of hot-rolled and cold-formed members of different steel grades subjected to pure compression, for $\chi_{CS} \geq 0.6$ cases.

Table 8: Design curves for the case of hot-rolled and cold-formed members subjected to pure compression

Cross-section	Fabrication process	λ_0	α					
			$f_y = 235$ (N/mm^2)	$f_y = 355$ (N/mm^2)	$f_y = 460$ (N/mm^2)	$f_y = 690$ (N/mm^2)	$f_y = 770$ (N/mm^2)	$f_y = 960$ (N/mm^2)
RHS and SHS	Hot-rolled	0.2	0.21	0.21	0.21	0.13	0.13	0.13
	Cold-formed	0.2	0.45	0.35	0.27	0.20	0.20	0.15

4.4. Influence of bending moment distribution

A leading parameter identified to influence the resistance of a beam-column member is the bending moment distribution represented by the ψ factor. This was expected since the member resistance is known to be greatly affected by the distribution of bending moment. Accordingly, many existing beam-column design formulas consider the ψ factor (or the C_m factor) as a governing parameter.

Some of the obtained numerical results are presented in O.I.C. format in Figure 33 along with the corresponding proposed curves. No matter what the load cases are, one may notice that members subjected to a triangular bending distribution exhibit a higher resistance than members subjected to a constant moment distribution. Higher interaction curves should then be derived when considering $\psi = 0$.

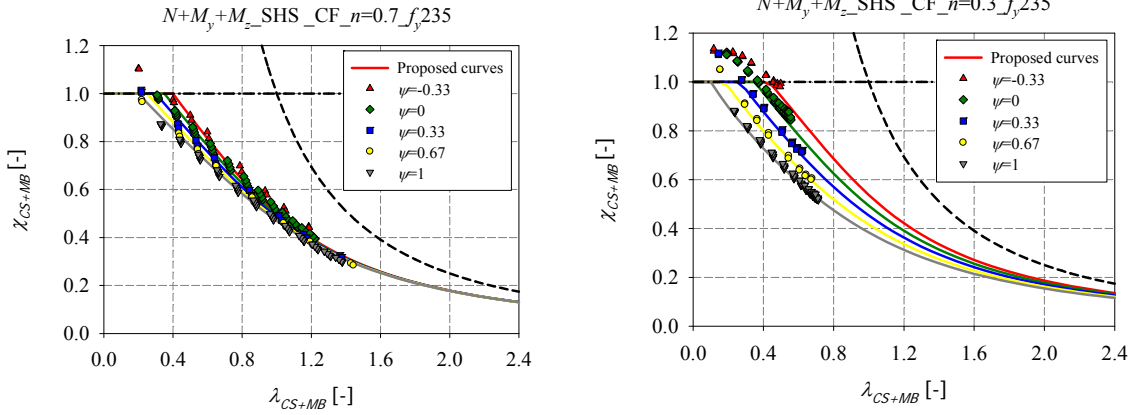


Figure 33: Numerical member results of cold-formed SHS tested under $N+M_y+M_z$

On one hand, a relation was established between the imperfection factor α_ψ and the imperfection factors $\alpha_{\psi=1}$, $\alpha_{\psi=0}$ for $\psi=0$ and $\psi=1.0$, respectively; on the other hand, between the end of plateau $\lambda_{0,\psi}$ and the ends of plateau $\lambda_{0,\psi=1}$, $\lambda_{0,\psi=0}$ for $\psi=1$ and $\psi=0$ as well according to Figure 34 and to the equations below:

$$\alpha_\psi = (\alpha_{\psi=1} - \alpha_{\psi=0})\psi + \alpha_{\psi=0} \text{ with } \alpha_\psi \geq 0 \quad (6)$$

$$\lambda_{0,\psi} = (\lambda_{0,\psi=1} - \lambda_{0,\psi=0})\psi + \lambda_{0,\psi=0} \text{ with } \lambda_{0,\psi} \geq 0 \quad (7)$$

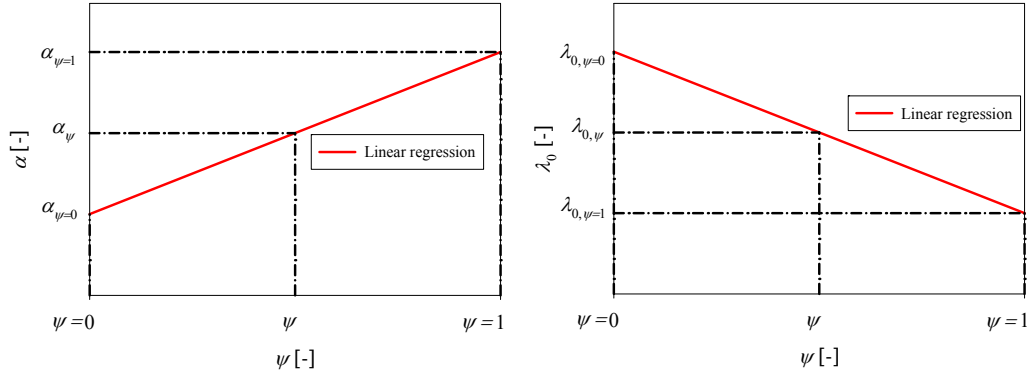


Figure 34: Linear regression between - a) $\alpha - \psi$ - b) $\lambda_0 - \psi$

4.5. Influence of axial compression

Figure 35 shows that the relative axial force ratio n defined as $n = N_{Ed} / N_{b,Rd} = (N_{Ed} / \chi \cdot N_{pl,Rd})$ or $N_{Ed} / \chi \cdot N_{eff,Rd}$ influences greatly the member resistance. For a high level of compression ($n = 0.7$), global buckling becomes determinant, leading to a wide range of generalized relative slenderness ($\lambda_{CS+MB} > 2$). Global buckling due to the high level of compression occurs before cross-section full yielding, resulting in the failure of the element due to member instability and not because of a lack of cross-sectional resistance.

However, for a lower level of compression ($n = 0.15$), results spans in a narrower range of slenderness. In such cases, bending is predominant but the members cannot experience lateral torsional buckling and exhibit a limited influence of global instability due to the low level of compression.

Accordingly, a leading parameter was defined according to Equation (8) and was used to sort the results regardless of the axial force ratio n . Non-dimensional and convenient factor η was first proposed by Taras (Taras A. 2011).

$$\eta = \frac{m}{n} = \frac{M / M_{pl}}{N / N_{pl}} \quad (8)$$

In Equation (8), N_{pl} and M_{pl} are the plastic cross-section resistance for pure axial force, and for pure bending moment about the weak or the strong axis, respectively; N and M_z are the ultimate axial force, and ultimate bending moment about the weak or the strong axis, respectively.

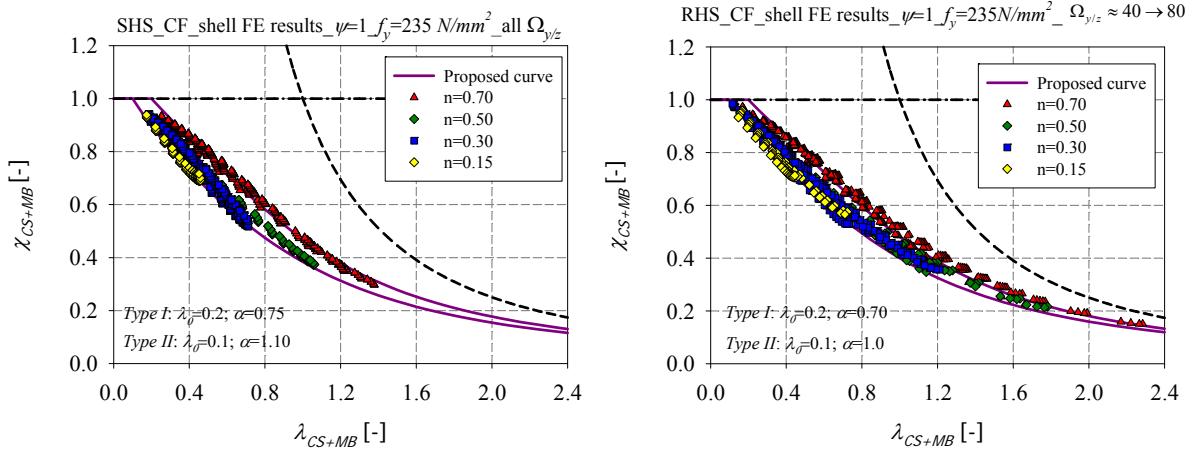


Figure 35: Numerical member results of cold-formed SHS of steel grade $f_y = 235 \text{ N/mm}^2$ tested under combined loading with different values of axial force ratio n – a) SHS – b) RHS

4.6. Influence of biaxiality degree

Figure 36 presents results of members tested under combined loading with a constant bending moment distribution. For each load case, 10 values of the degree of biaxial bending were adopted varying from $\alpha_{biaxiality} = 0^\circ$ to $\alpha_{biaxiality} = 90^\circ$ with a range of 10 degrees. The M_y / M_z ratio is clearly seen to be another key parameter for the derivation of appropriate design curves.

As can be seen in the figures, quite limited scatter is observed for square sections due to the symmetrical geometry of the sections. However, larger scatters are observed in the case of rectangular sections. The resistance of the member in this case is largely influenced by the degree of biaxial bending: For cases where weak-axis bending takes over strong-axis bending ($\alpha_{biaxiality} > 45^\circ$), the O.I.C. resistance curves begin to increase again after a progressive drop starting from the combined loading $N+M_y$ alone. When M_z is applied to an $N+M_y$ loading with a small proportion ($\alpha_{biaxiality} < 45^\circ$), instability is increased if compared to the $N+M_y$ loading; nevertheless, when M_z becomes dominant, the section becomes more stable.

Consequently, one curve was proposed for the case of square sections regardless of the degree of biaxial bending for sake of simplicity. The adopted curve was derived lower than the one adopted for the case of $N+M_y$ and $N+M_z$. In contrast, different curves were proposed for the case of rectangular sections depending on the $\alpha_{biaxiality}$ -factor, since it has a significant impact on the resistance of rectangular sections. The factor $\alpha_{biaxiality}$ is equivalent to the derived factor $\Omega_{y/z}$ and can be calculated following Equation (9).

$$\Omega_{y/z} = \arctan\left(\frac{m_z}{m_y}\right) = \arctan\left(\frac{M_z / M_{pl,z}}{M_y / M_{pl,y}}\right) \quad (9)$$

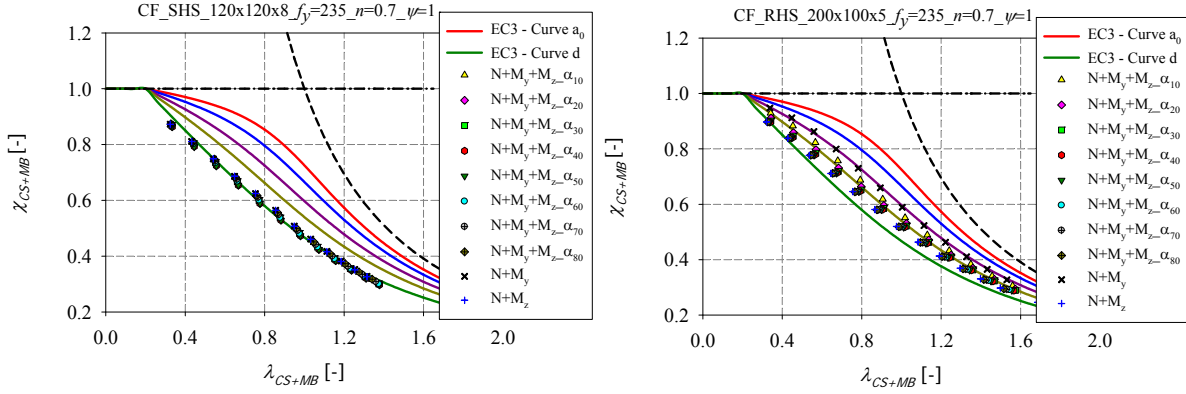


Figure 36: Numerical member results obtained for different degrees of biaxial bending values and $\psi = 1$ for – a) cold-formed SHS – b) cold-formed RHS

4.7. Influence of cross-section shape and slenderness

The cross-section shape (rectangular or square) influenced the member resistance. Special attention was given so that the proposed formulae exhibit no discontinuities. Accordingly, the h/b ratio was introduced in the derived formulae for beam-column resistance as illustrated in Figure 37, where $\alpha_{h/b=1}$ represent the imperfection factors proposed for the case of square sections, $\alpha_{h/b \geq 1.3}$ correspond to the imperfection factors proposed for the rectangular European sections and $\alpha_{1 < h/b < 1.3}$ correspond to the imperfection factors of invented sections having aspect ratios ranging from 1 to 1.3.

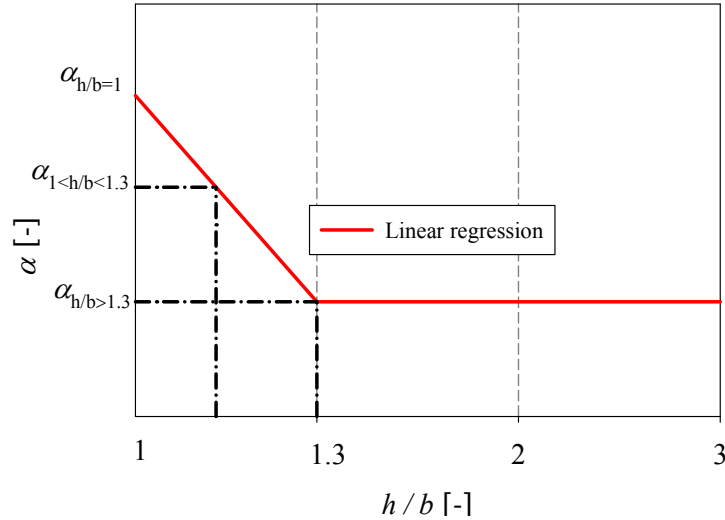


Figure 37: Linear transition between $\alpha - h/b$

5. Conclusions and future developments

A total of 12 beam-column tests, consisting of hot-rolled and cold-formed RHS and CHS members under eccentrically-applied compression has been carried out and detailed in this paper. Results relative to material response, residual stresses measurements and careful determination of initial geometrical imperfections were reported. The (imperfect) initial geometry was measured along the whole column by means of two different procedures. The first method relied on the use of a set of equally spaced LVDTs displaced on each specimen's plates; the second method consisted in scanning the specimen's plates by means of a laser Tracker *AT401*. Residual stresses were examined by mean of the sectioning technique and compared to the stresses obtained by the electrical strain gauges.

Besides, numerical shell models simulating the test conditions as closely as possible were developed. For both the present test series and another one from the literature, it was found that the F.E. models were capable of replicating accurately the response and resistance of the experiments.

Accordingly, the validated F.E. models have been further used in extensive numerical studies, and a database comprising more than seventy thousand results was built consecutively, for hot-rolled and cold-formed members. These results have served to assess the application of the O.I.C. to hollow section beam-column resistance.

Acknowledgements

CIDECT, by means of financial and technical support within research project "HOLLOPOC", is gratefully acknowledged.

References

- Ayrton W.E. & Perry J. (1886). "On Struts." *The engineer*, Vol.62.
- Boissonnade N., Greiner R. Jaspert J.P., Lindner J. (2006). "Rules for Member Stability in EN 1993-1-1; Background documentation and design guidelines". Eds. Mem Martins, Portugal, ECCS – ISBN 92-9147-000-84, Vol. 119.
- Boissonnade N., Nseir J., Saloumi E. (2013). "The Overall Interaction Concept: An Alternative Approach to the Stability and Resistance of Steel Sections and Members." *Proceedings of the Annual Stability Conference, Structural Stability Research Council*, St. Louis, Missouri.
- CEN (Comité Européen de Normalisation. (2005). "Eurocode 3: Design of Steel Structures, Part 1-1: General rules and rules for buildings (EN 1993-1-1)", Brussels.
- Epiney V. (2015). "Résistance et Stabilité Des Éléments En Acier Fléchis et Tendus." *Master HES-SO*, Ingénierie du Territoire MIT.
- Greish & ULg (1999). "FINELg, Non Linear Finite Element Analysis Software." *University of Liege - The engineering office Greisch*
- Nseir J. (2015). "Development of a New Design Method for the Cross-Section Capacity of Steel Hollow Sections." University of Liege, Belgium.
- Nseir J, Hayeck M., Saloumi E., Boissonnade N. (2016). "Influence of imperfections on the local buckling response of hollow structural shapes". *Proceedings of the Annual Stability Conference, Structural Stability Research Council*, Orlando, Florida, April 12-15.
- Semi-Comp (2007). "Plastic member capacity of semi-compact steel sections – a more economic design (Semi-Comp)". 2007. *Final report (01/01/06 – 30/06/07) – RFCS – Steel RTD (Contract RFS-CR-04044)*.
- Taras A. (2011). "Contribution to the development of consistent stability design rules for steel members". *Graz University of Technology, Faculty of Civil Engineering*.